Physics Basis, Optimization, and Control for Integrated 3D Edge Long-pulse Tokamak Scenarios
DE-SC0020413

December 1, 2022

PI: Professor Zhihong Lin
University of California, Irvine

I. Accomplishments

The aim of this project with international collaborations (PI: J.-K. Park of Princeton Plasma Physics Laboratory) is to develop a unified physics basis and predictive capability for the control of edge-localized modes (ELMs) with optimized non-axisymmetric (3D) fields, by leveraging the unique research capabilities of international KSTAR tokamak in Korea. At the University of California, Irvine, we use a fusion simulation code GTC to study the effects of the 3D magnetic fields (including both magnetic islands and stochastic magnetic field lines) on microturbulence. We focus on the effects of 3D equilibrium on turbulent and neoclassical transport that leads to ELM suppression.

During the project period, the UCI team of this collaboration has made significant progress in understanding turbulent transport in 3D geometry including both tokamaks with RMP and stellarators. Four UCI postdoctoral researchers, Drs. Javier Nicolau, Gyungjin Choi, Pengfei Liu, and Xishuo Wei were partially supported by this project and collaborating with the entire project team. We have published 4 journal papers and gave several invited talks, as listed in Section II. Publications and Invited Talks.

This project advance physics understand of 3D effects on microturbulence, specially effects of magnetic islands. It will contribute to the DOE SciDAC ISEP project in the area of GTC development for general 3D geometry capability, rigorous verification and validation, and readiness for the emerging exascale computing. Through collaborations with computational scientists, the project helps to advance high performance computing in the area of GPU acceleration, linear solver, and data management.

In the followings, we highlight recent accomplishments in the following tasks carried out by GTC simulations:

- **A.** GTC simulation of microturbulence in KSTAR with RMP
- **B.** Effects of RMP on neoclassical ambipolar electric field, collisionless damping of zonal flow, and damping of toroidal rotation in DIII-D

A. GTC simulation of microturbulence in KSTAR with RMP

GTC simulations find turbulent transport modulated by GAM with RMP in KSTAR #23134. The plasma profiles are from EFIT reconstruction and RMP 3D magnetic field with small magnetic islands is from M3D-C1 simulations (Fig.1). The island width is about 1cm, which is smaller than thermal ion guiding center orbits width.

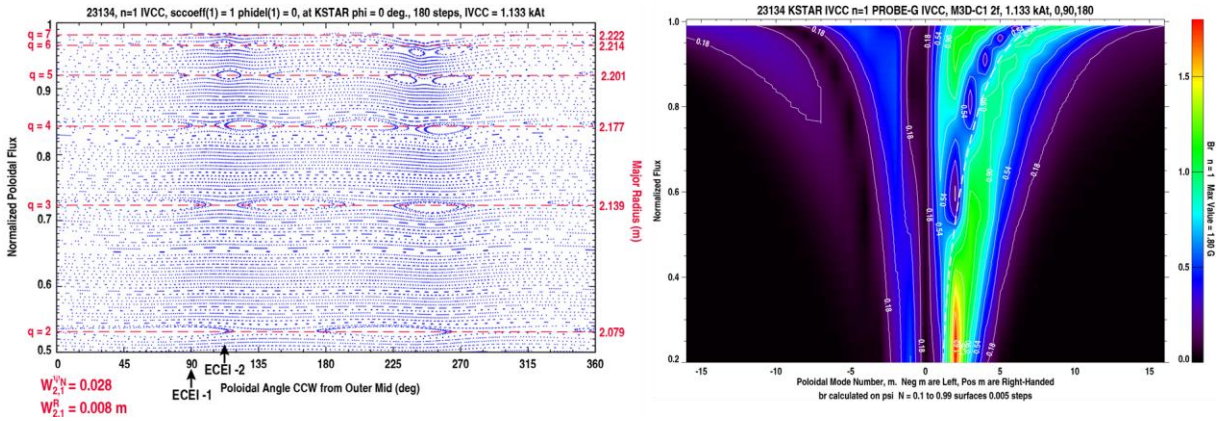

Figure 1. *Magnetic flux-surface vs poloidal angle (left panel) showing small magnetic islands separated by closed flux-surfaces, and radial profiles of poloidal harmonics of RMP (right panel).*

GTC simulation finds dominant instability is trapped electron mode (TEM) with $k_\perp \rho_s > 1$ in linear phase. In nonlinear phase (Fig. 2), there is an inverse spectral transfer to small k_θ (Fig.3) and the turbulence spreads radially. TEM is saturated by zonal flow at $e\phi_{\rm rms}/T_e \sim 2\%$. The transport is $\chi_i \sim \chi_e \sim 5\chi_{\rm gB}$. Temporal intermittency (i.e., modulation) of transport appears due to turbulence-GAM interaction (Fig. 4).

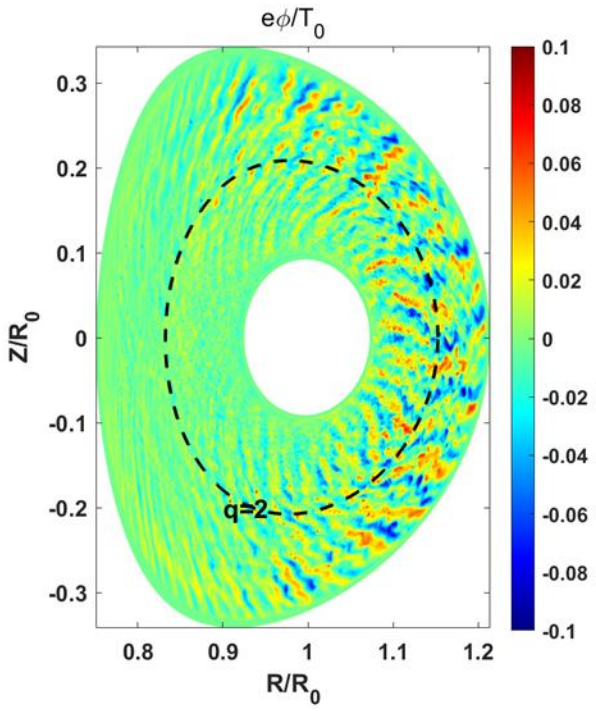

Figure 2. *Poloidal contour plot of electrostatic potential of TEM turbulence in KSTAR shot #23134 with RMP.*

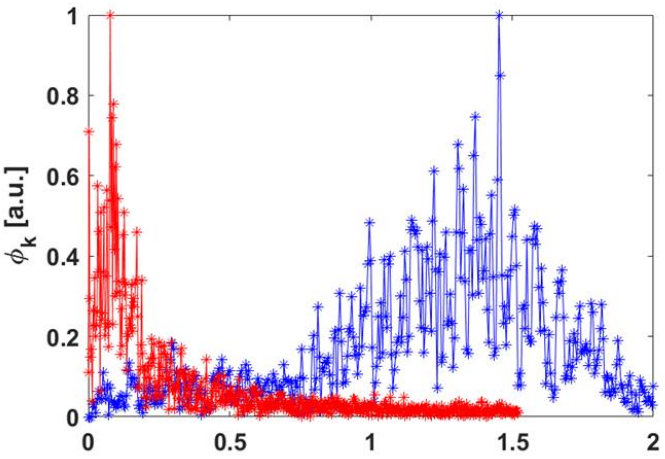

Figure 3. *Inverse cascade of the poloidal wave number from linear (blue) to nonlinear (red) in TEM turbulence in KSTAR shot #23134 with RMP.*

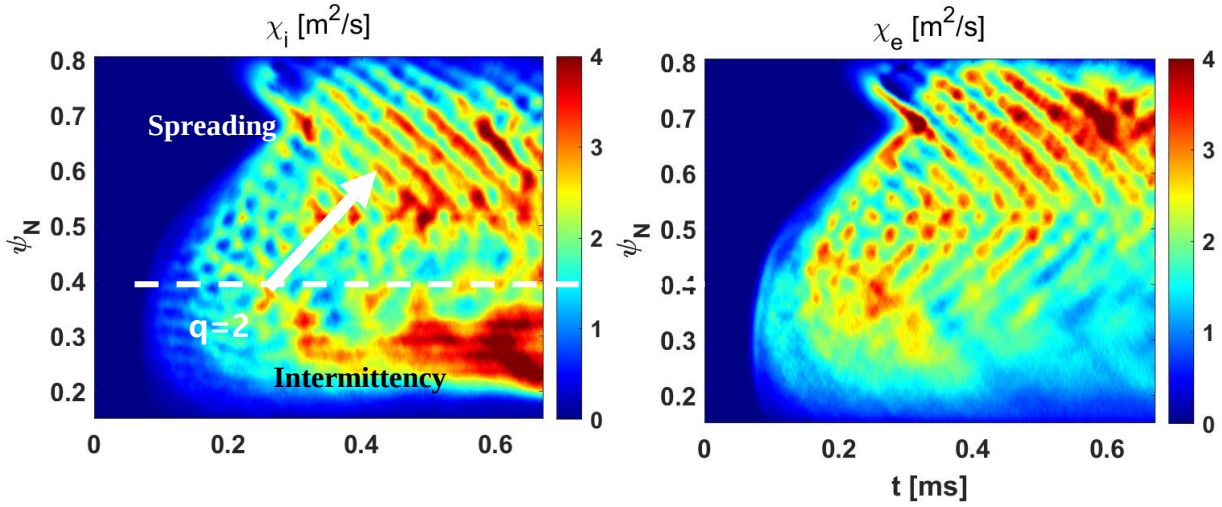

Figure 4. *Ion and electron heat conductivities as function of radial and time in KSTAR shot #23134 with RMP showing turbulence spreading and modulation of TEM turbulence by GAM.*

The main activities of turbulence dynamics and transport is in the $q \gtrsim 2$ region, completely different from location of linear eigenmode peaking at q=1.4 surface. The GAM-induced oscillation of structure of zonal flow shearing rate is anti-correlated with that of turbulence amplitude. Nonlinear evolutions of turbulence and zonal flow show radial inversion symmetry with respect to q=2 island.

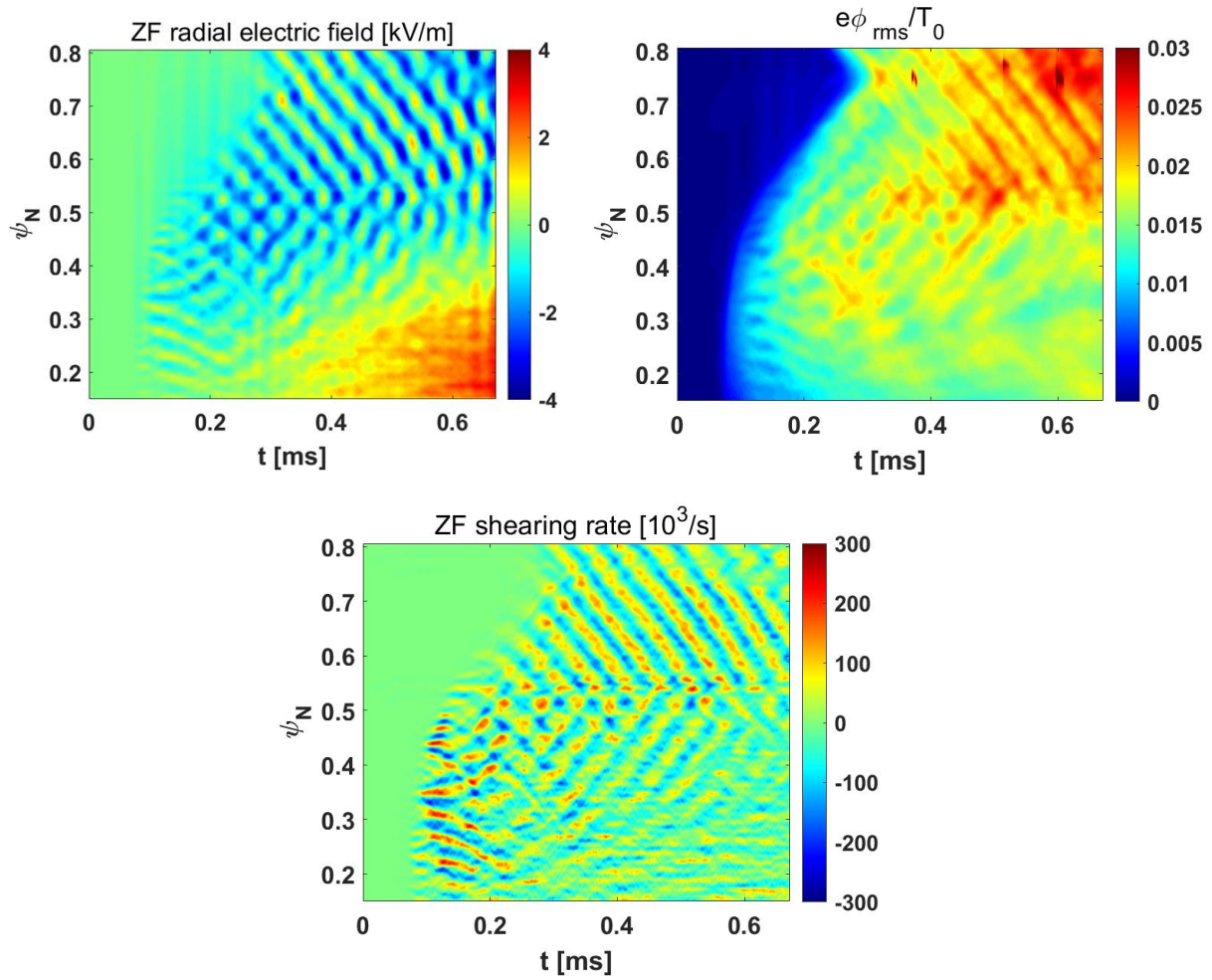

Figure 5. *Zonal mode electric field, potential, and shearing rate as function of radial and time in KSTAR shot #23134 with RMP showing turbulence spreading and modulation of TEM turbulence by GAM.*

These GTC nonlinear simulations shows that RMP in KSTAR #23134 changes qualitative features of turbulence and transport. However, it doesn't make a significant quantitative change in average. This result is consistent with small RMP-induced island size found from M3D-C1 simulations. We have discussed with collaborators SeongMoo Yang (PPPL) and SangKyeun Kim (PU) to select more interesting cases in KSTAR discharges with large islands generated by RMP. Three shots have been considered:
- #19118: RMP L-mode plasma, Te flattening at q=2 and rotation locking observed after RMP.
- #26004: RMP after H-mode transition, hysteresis with RMP modulation after ELM suppression.
- #26027: Increasing RMP before H-mode transition, near-threshold behaviors (LCO) shifted to later time.
All three shots show interesting phenomena to be studied, but we focus on #19118 where we can observed clear profile flattening, a symptom of large island. Primitive ECEI analysis also shows X-point-like structure (Fig. 6).

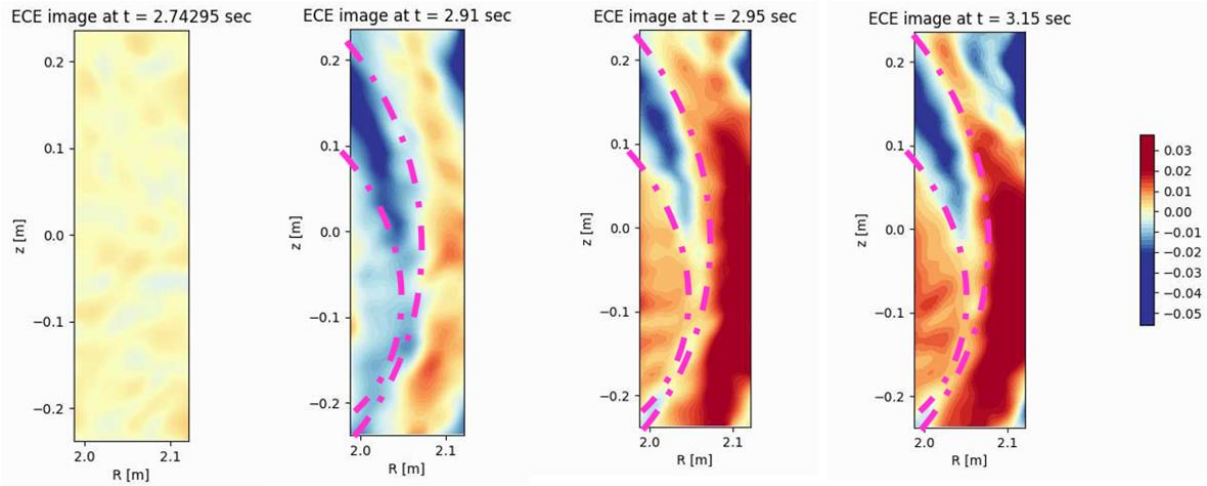

Figure 6. *ECEI measurements in #19118 by Heo Jinyoung (UNIST) in collaboration with SeongMoo Yang.*

B. Effects of RMP on neoclassical ambipolar electric field, collisionless damping of zonal flow, and damping of toroidal rotation in DIII-D

We now study effects of the RMP on electron particle fluxes Γ_e using the equilibrium and plasma parameters of the DIII-D discharge #158103. Since the main island chains at the $q = 4$ rational surface is close to the separatrix, high energy trapped ions can cross the separatrix into the SOL. These lost ions can have significant effects on the radial electric fields near the separatrix even without applying RMP. The focus of this paper is to calculate the additional effects of the RMP, on top of the lost ions and the electrons. Therefore, we assume that ion and electron have already achieved ambipolarity before RMP is applied. Also, only the electrons are simulated, assuming that effects of the RMP on the ion transport is much smaller than the electron transport.

We use the rigid rotation case to verify the effects of the RMP on neoclassical transport, where the particle fluxes in the presence of the RMP are measured by $\Gamma_e = \left\langle \int \left(\mathbf{v_d} + v_\parallel \frac{\delta \mathbf{B}}{B_0} \right) \cdot \nabla \psi \, \delta f_e \, d^3 v \right\rangle$. Define the non-ambipolar particle flux induced by the RMP $\Delta\Gamma_e \equiv \Gamma_{RMP} - \Gamma_0$, where Γ_{RMP} and Γ_0 are the neoclassical electron particle fluxes with and without the RMP. The neoclassical particle flux in axisymmetric tokamak Γ_0 is intrinsically ambipolar. However, Γ_{RMP} is not ambipolar and $\Delta\Gamma_e$ can induce a change of ambipolar electric field to restore the ambipolarity, similar to the neoclassical transport in stellarators.

Fig. 7(a) shows the time history of volume-averaged electron particle fluxes Γ_e around 8/2 and 7/2 island regions. The electron particle fluxes reach a steady state after a few collision times $\tau_e = 1/\nu$. In the simulation without the RMP, there is no obvious difference between the Γ_e in these two regions. However, in the simulation with the RMP, compared with the 7/2 island, the wider 8/2 island induces a much larger increase of electron particle flux $\Delta\Gamma_e$ at steady state $t = 40\,\tau_e$. The $\Delta\Gamma_e$ induced by the 8/2 island is comparable to the Γ_0, but is much smaller than the turbulent transport level and therefore does not contribute to the density pump out. However, the non-ambipolar particle fluxes can induce an ambipolar electric field.

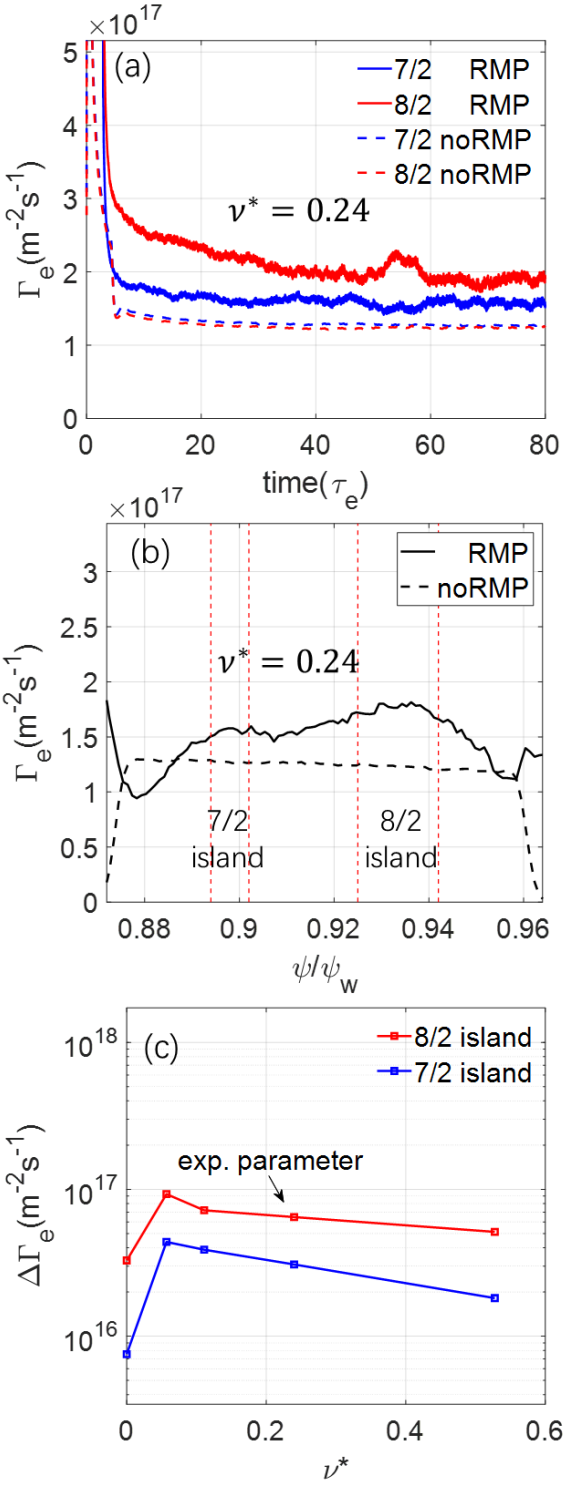

Figure 7. *Neoclassical electron particle flux in rigid rotation case. (a) Time history of Γ_e at 7/2 and 8/2 island region in simulations with and without RMP. (b) Γ_e profile averaged over $t = [40,80]\,\tau_e$ in simulations with and without RMP. Vertical dashed lines represent island separatrices. (c) Dependence of $\Delta\Gamma_e$ on collision frequency ν^* at 7/2 and 8/2 island region.*

Fig 7(b) shows the Γ_e radial profiles averaged over $t = [40,80]\ \tau_e$ in the simulations with and without the RMP. Three regions, the 7/2 island region ($q = 3.44\sim3.55$), the 8/2 island region ($q = 3.84\sim4.15$), and the non-resonant region ($q = 3.55\sim3.84$), are separated by the island separatrices. The larger 8/2 island induces a much larger $\Delta\Gamma_e$ than that in the 7/2 island region and in the non-resonant region, which suggests that the non-ambipolar electron particle flux is mostly driven by the resonant component of the RMP.

Fig 7(c) shows the $\Delta\Gamma_e$ in the simulations varying the collision frequency $\nu^* = [0, 0.5]$ in the two island regions. The $\Delta\Gamma_e$ in the collisionless case is much smaller than that in the simulations with collisions, which indicates that the flutter transport due to magnetic stochasticity is not dominant. The $\Delta\Gamma_e$ in both the 7/2 and 8/2 island regions slightly decreases with the collision frequency in the banana regime.

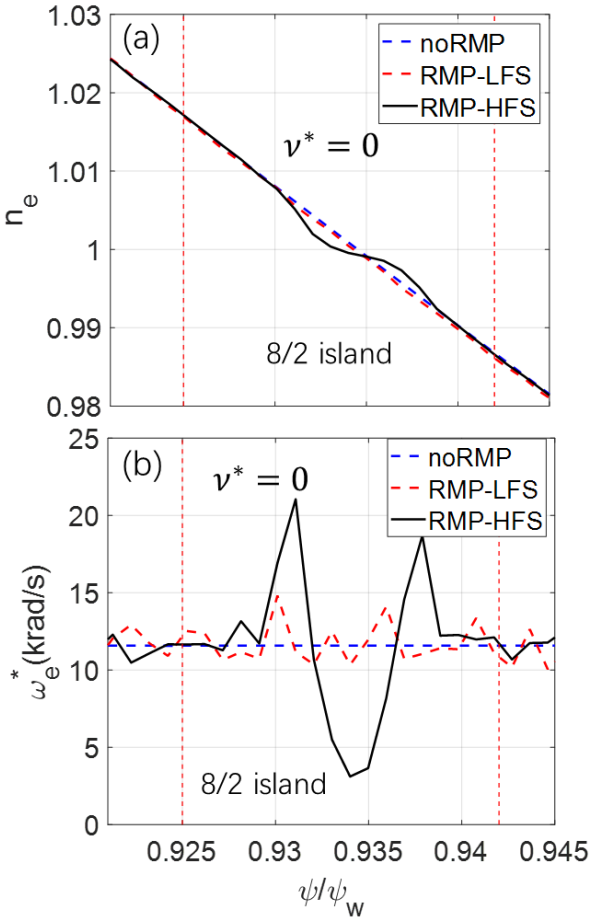

Figure 8. *Electron density profiles n_e (panel a) and diamagnetic frequency ω_e^* profiles (panel b) in rigid rotation case in 8/2 island region in collisionless simulations after profile relaxation. Red-dashed and black line are density profiles on low field side and high field side with RMP. Blue-dashed line is density profile without RMP. Vertical dashed lines represent island separatrices.*

Fig 8(a) shows the relaxation of electron density profiles in the 8/2 island region in the collisionless simulations with and without the RMP. On the high field side, the electron density profile is locally flattened inside the 8/2 island region and reach the steady state after some bounce times. On the low field side, the electron density profile is less affected by the RMP, because the trapped particles on the low field side do not follow the field line around the magnetic island. In the collisional simulations, the collisions could further modify the density profiles.

Fig 8(b) shows the relaxation of electron diamagnetic frequency $\omega_e^* = -\frac{1}{qn_e e}\frac{\partial n_e T_e}{\partial \psi}$ profiles in the 8/2 island region in the collisionless simulations with and without the RMP. On the low field side, the electron diamagnetic frequency is only slightly affected by the RMP, which is consistent with the change of density profile on the low field side. On the high field side, the electron diamagnetic frequency is significantly changed across the 8/2 island region, because the density profile is flattened locally.

We now use experimental n_e and T_e profiles. Two sets of simulations are carried out with or without the RMP. The first set uses the experimental n_e profile and a uniform $T_e = T_e(q = 4)$, thus $\kappa_t = 0$. The second set uses both the experimental n_e and T_e profiles as the equilibrium profiles.

Fig. 9 shows the steady state Γ_e profiles in the simulations. In the simulations without the RMP, the ambipolar Γ_e in the case with experimental T_e (κ_t>0) is slightly smaller than that in the uniform T_e (κ_t=0) case, which qualitatively agrees with the standard neoclassical theory. In the simulations with the RMP, both uniform T_e and experimental T_e profiles can induce the non-ambipolar particle fluxes $\Delta\Gamma_e$. We rewrite the non-ambipolar particle flux $\Delta\Gamma_e = D_0(\kappa_n + \beta\kappa_t)$, where D_0 is the transport coefficient in the uniform T_e (κ_t=0) case, β denotes the ratio between the contribution from temperature and density gradients. We find that $\beta = 0.56$, which is qualitatively consistent with the NTV theory.

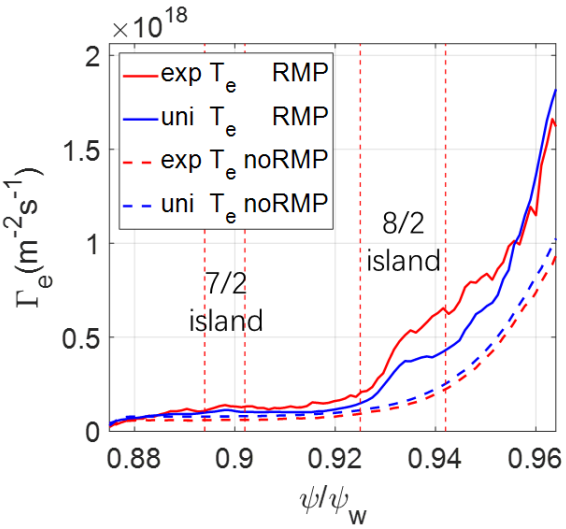

Figure 9. *Electron particle flux Γ_e profiles from neoclassical simulations using experimental density profile, experimental T_e (red line) or uniform T_e profiles (blue line), with (solid line) and without (dashed line) RMP. Vertical dashed lines represent island separatrices.*

The neoclassical simulations use the RMP equilibrium calculated by the M3D-C1, which could have a large uncertainty in the magnetic island width. Therefore, we perform a sensitivity study for the RMP amplitude α. Fig. 10 shows the dependence of $\Delta\Gamma_e$ on the α on the q=4 surface from GTC neoclassical simulations using experimental equilibrium profiles, where α_0 is the original RMP amplitude calculated by the M3D-C1. It is clear that $\Delta\Gamma_e$ follows a quadratic relation with α, i.e., the non-ambipolar flux is proportional to the magnetic island width.

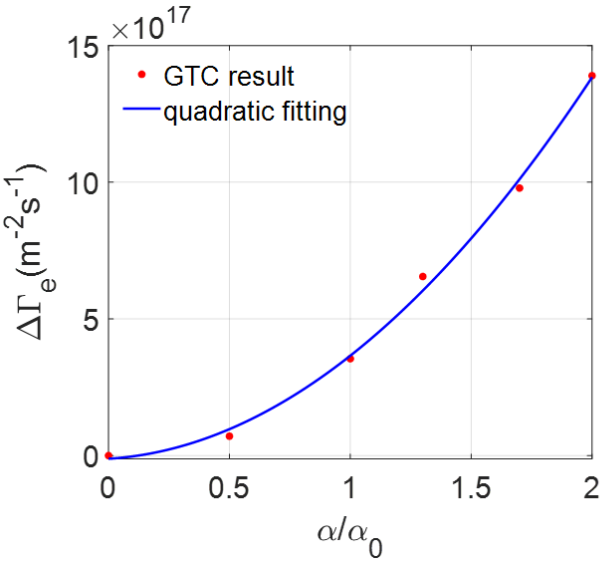

Figure 10. *Dependence of non-ambipolar electron particle flux* $\Delta\Gamma_e(q=4)$ *on RMP amplitude* α *from neoclassical simulation. The blue line is a quadratic fit.*

The effects of equilibrium electric field E_r on the neoclassical transport is now studied. During the time scale of the ELM suppression (~1 ms), the equilibrium density and temperature profiles do not change much, but the equilibrium electric field E_r can change significantly, which can affect the neoclassical and turbulent transport.

Fig. 11(a) shows the radial profiles of the experimental equilibrium E_r on the outer midplane during the ELMing (3796ms) and ELM suppression (3050ms) in the DIII-D discharge #158103. In this section, these two E_r profiles, together with the n_e and T_e profiles at 3050 ms, are used as the equilibrium. The 8/2 island width is much smaller than the typical equilibrium inhomogeneity scale length, which allows us to use the 1D equilibrium electric field.

First, we verify the effects of the equilibrium electric field E_r using the uniform κ_n and T_e profiles with the value at the $q=4$ flux surface. Uniform $E_\psi = -\frac{\partial\phi}{\partial\psi}$ profiles (rigid rotation case) or experimental E_r profiles are used in the simulations separately. Fig 11(b) shows the $\Delta\Gamma_e$ near the $q=4$ surface at the steady state of neoclassical simulations using the equilibrium with the RMP and the uniform electric field E_ψ. Here, we use $E_N \equiv -\frac{\partial\phi}{\partial\psi} / \frac{T_\alpha}{q_\alpha}\kappa_n$ to represent the amplitude of the electric field, which corresponds to the ratio between the $\mathbf{E}\times\mathbf{B}$ and diamagnetic flows. The E_N values of 2.9 and -0.22 correspond to the local value of the electric field during the ELMing and the ELM suppression, respectively. The value of $E_N = -1$ corresponds to the toroidal rotation frequency $\Omega_{te}=0$. In the rigid rotation case, when $E_N=-1$, the $\Delta\Gamma_e$ is three orders of magnitude smaller than the neoclassical particle flux without the effect of RMP. When the $E_N \neq -1$, the absolute value of the $\Delta\Gamma_e$ begins to increase, which can change the radial electric field and damp the rotation, in qualitative agreement with the neoclassical theory predicting the toroidal flow damping by the toroidal viscosity due to the 3D magnetic fields.

In the simulations using the experimental E_r profiles without the RMP, the shear of the equilibrium electric field E_r has little effects on the Γ_e, because the electrons banana orbit width is much smaller than the radial scale length of the electric field. In the simulations with the RMP, both the experimental E_r profiles during the ELMing and the ELM suppression are found to induce additional positive $\Delta\Gamma_e$ when compared with the

uniform electric field. The value of $\Delta\Gamma_e$ in the simulation with the E_r during the ELMing is much larger than that during the ELM suppression, which indicates that the rotation damping during the ELMing is much larger than that during the ELM suppression.

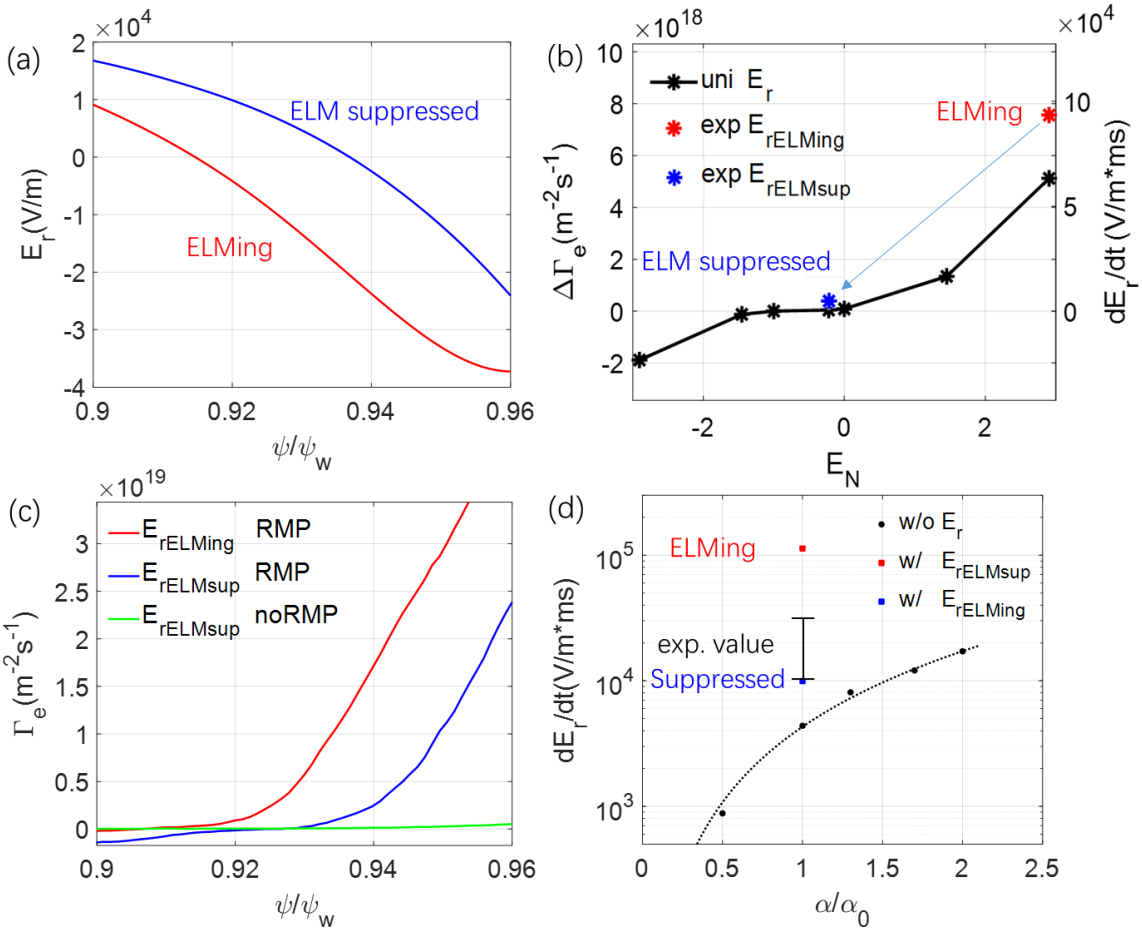

Figure 11. *(a) Equilibrium electric field E_r profiles of DIII-D for 158103 discharge during ELMing and ELM suppression. (b) Dependence of non-ambipolar particle flux $\Delta\Gamma_e$ on electric field amplitude E_N at $q = 4$ flux surface in simulations with uniform and experimental E_r profiles, using the uniform κ_n and T_e profiles. (c) Profiles of Γ_e at steady state of neoclassical simulations with E_r profiles during ELMing (blue line) and ELM suppression (red line), and without RMP (yellow line), using experimental density and temperature profiles. (d) Dependence of time rate of change of E_r at $q = 4$ flux surface on RMP amplitude α from simulations without equilibrium E_r and with equilibrium E_r during ELMing and ELM suppression. Error bar represents experimental value with 50% uncertainty range.*

Finally, to compare with the experimental measurements of rotation damping, we carry out simulations using the experimental n_e, T_e, and the two E_r profiles. Fig 11 (c) shows the Γ_e profiles at the steady state of these neoclassical simulations with or without the RMP. In the simulations without the RMP, the shear of E_r has little effects on the Γ_e, same as the simulation results in the rigid rotation case. In the simulations with the RMP, the E_r profile during the ELMing induces a much larger non-ambipolar particle flux $\Delta\Gamma_e$ than that during the ELM suppression. This indicates that the non-ambipolar particle flux $\Delta\Gamma_e$ can drop drastically during the ELM suppression, which is mainly due to the rapid change of the equilibrium electric field E_r. The sensitivity of the electron flux on the equilibrium electric field indicates that some electron orbits become stochastic due to the RMP.

We now calculate the damping rate of the toroidal rotation by calculating the time rate of change of the electric field E_r using the non-ambipolar particle flux $\Delta\Gamma_e$ measured in the steady state of the neoclassical simulations in the previous sections. Combining the gyrokinetic Poisson's equation and guiding center continuity equation, the quasi-neutrality condition takes the form,

$$\frac{dE_\psi}{dt}\left\langle\frac{|\nabla\psi|^2}{B^2}\right\rangle = -\frac{1}{m_i n_i c^2}\sum_s q_s\left\langle\int d^3v\ f_s\left(\mathbf{v_d}+\mathbf{v_E}+v_\parallel\frac{\delta\mathbf{B}}{B_0}\right)\cdot\nabla\psi\right\rangle. \quad (4)$$

Here, the subscript s denotes the particle species (i for ion and e for electron). The flux-surface-averaged polarization current on the left hand side cancels out with the guiding center current on the right hand side. The relation between $E_\psi \equiv -\frac{\partial\phi}{\partial\psi}$ and radial electric field E_r is $E_r = E_\psi|\nabla\psi|$. The Γ_i and Γ_e are assumed to be ambipolar without the effects of RMP. For the non-ambipolar particle fluxes, only the electron contribution is taken into account by assuming that the ion contribution is negligible. Equation (4) is then used to calculate the damping rate of the toroidal rotation.

Fig. 11(d) shows the damping rate at the $q = 4$ flux surface calculated from the simulations using the experimental n_e, T_e and the two experimental E_r profiles. When comparing simulation results with the experimental measurement of the damping rate during the ELM suppression, two aspects of uncertainty should be considered. The first one comes from the MHD simulations of the RMP amplitude α. In the α amplitude scanning, the damping rate is about one third of the experimental level when $\alpha = \alpha_0$, but reaches the experimental level when using $\alpha = 2\alpha_0$. The second uncertainty comes from the rapid change of the E_r during the transition from ELMing to ELM suppression. The damping rate is proportional to the non-ambipolar particle fluxes $\Delta\Gamma_e$, which depends on the E_r amplitude and shear, as shown in Fig. 11(b). From the ELMing and ELM suppression state, the damping rate decreases drastically due to the change of the equilibrium electric fields. This result is consistent with the experiment, in which the toroidal rotation experiences a large torque before the onset of the ELM suppression, followed by relatively small torque after the transition to the ELM suppression state. The simulated damping rate during the ELM suppression qualitatively agrees with the experimental value.

To understand the RMP effects on zonal flow dynamics, collisionless zonal flow damping and geodesic acoustic mode (GAM) are simulated by using two types of the 3D RMP fields. Besides the RMP equilibrium described above, another equilibrium is obtained from the ideal MHD code VMEC, which includes only the non-resonant response of the RMP and thus preserves the closed flux surfaces. For the VMEC equilibrium, an electrostatic version of the fluid-kinetic hybrid electron model is used to treat the kinetic electrons. In this model, the perturbed electron distribution function is represented by $\delta f_e = \delta f_e^{(0)} + \delta h_e$, where $\delta f_e^{(0)}$ is the adiabatic response to the non-zonal electric field, and δh_e is the nonadiabatic response. For the M3D-C1 equilibrium with magnetic islands, the drift kinetic equation DKE is used for solving the electron perturbed distribution function. Both the zonal and nonzonal electric field components are solved together in the presence of magnetic islands. The ion dynamics is simulated by solving the standard gyrokinetic equation. The radial particle flux in this section is defined as

$$\Gamma_s = \left\langle\int d^3v\ \delta f_s(\mathbf{v_d}+\mathbf{v_E})\cdot\nabla\psi\right\rangle, (s=i,e)$$

for the ions and electrons in the hybrid model using the VMEC equilibrium, and

$$\Gamma_s = \left\langle\int d^3v\ \delta f_s\left(\mathbf{v_d}+\mathbf{v_E}+v_\parallel\frac{\delta\mathbf{B}}{B_0}\right)\cdot\nabla\psi\right\rangle, (s=i,e)$$

for the ions and the electrons in the DKE model using the M3D-C1 equilibrium.

In these simulations, a flux-surface-averaged ion guiding center density perturbation is initiated to generate the zonal flows. The radial profile of the zonal flows is set to be a sin-function with a radial wavevector $k_r\rho_i = 0.4$. The density perturbation is set to be zero at the inner and outer boundaries of the simulation

domain $\psi = [0.90,0.97]\ \psi_w$. Simulations in this section use uniform equilibrium density and temperature profiles for both ions and electrons ($T_i \approx 1.7T_e$), corresponding to the local parameters at the $q = 4$ surface of the DIII-D experiment.

Firstly, we study effects of kinetic electrons by using gyrokinetic ions and fluid-kinetic hybrid electron model. The time evolution of the radial electric field E_r of the zonal flows on the $q = 4$ surface using the VMEC equilibrium with various RMP amplitudes (without RMP, or amplified by 1, 2, 5, 10 times) are shown in the Fig. 12(a). We can see that the radial electric field evolves with a finite frequency, i.e., damped GAM oscillation, and then reaches a steady state. In the simulation without the RMP, the zonal flow residual level is very close to that in the simulation only with the adiabatic electrons, which indicates that the effect of the kinetic electrons in zonal flow damping could be neglected without the RMP. The zonal flow residual level is much higher than the Rosenbluth-Hinton theory, which neglects shaping effect and finite aspect ratio.

In the simulations with different RMP amplitudes, the change of the residual flow ΔE_r is defined as the difference between the E_r and that in the simulation without the RMP at the same simulation time. The ΔE_r is found to depend quadratically on the RMP amplitude, which is consistent with that in the section 3.3. As shown in the fig 12(b), when the RMP amplitude is amplified by 10 times, the change of the residual flow ΔE_r at $t = 50\ R_0/c_s$ could reach 60%, which is three times larger than that in the simulation with only the adiabatic electrons. Here, the R_0 is the major radius at magnetic axis, $c_s = \sqrt{T_e/m_i}$ is the speed of ion acoustic wave.

Fig 12(c) and (d) show the time history of radial particle fluxes for the ion Γ_i and electron Γ_e in simulations without RMP and RMP×10. The Γ_i oscillates with the GAM frequency before $t = 10\ R_0/c_s$. Subsequently, the Γ_i gradually drops to a much lower level in both the simulations. On the other hand, the Γ_e has a strong oscillation with the GAM frequency before $t = 10\ R_0/c_s$, which is mainly due to electrons adiabatic response to the non-zonal electric fields ($m \neq 0, n = 0$), through the product of $\delta f_e^{(0)}$ with $\mathbf{v_d}$. The Γ_e stays at a high level during $t = 10\sim35\ R_0/c_s$ in the simulation with RMP×10, but is always very small after $t = 12\ R_0/c_s$ in the simulation without the RMP. This indicates that electron orbits could become stochastic due to the large RMP amplitude, and the residual flow damping is mainly induced by electrons, rather than ions. This result may have implications on zonal flow dynamics in the tokamaks with ripple fields and in the stellarators.

Finally, to study the effects of the RMP islands on zonal flow damping, the M3D-C1 equilibrium is used. The time evolution of the radial electric field E_r of the zonal flows with various RMP amplitudes (without RMP, with RMP and RMP×2) are shown in the fig 13(a). In the simulation without the RMP, the residual zonal flow is close to the result of the VMEC equilibrium within a difference of 20%, which could be due to the differences in the equilibrium and simulation model. The GAM oscillation (during 0~5 R_0/c_s) is strongly damped when the RMP amplitude increases. The residual flow in the simulation with the RMP×2 amplitude with the magnetic islands has a 30% reduction, which is much larger than that in the simulation using the VMEC equilibrium without magnetic islands.

Fig 13(b) shows the ion and electron particle fluxes in simulations without RMP and with RMP×2 using the M3D-C1 equilibrium with magnetic islands. In the simulation without the RMP, the electron particle flux Γ_e oscillation is strong during the GAM oscillation. In the simulation with RMP×2, the electron particle flux Γ_e changes strongly at the early time ($< 2\ R_0/c_s$), which is mainly due to the magnetic flutter effect from the fast parallel motion of the elections. The GAM oscillation is then strongly damped by this radial transport.

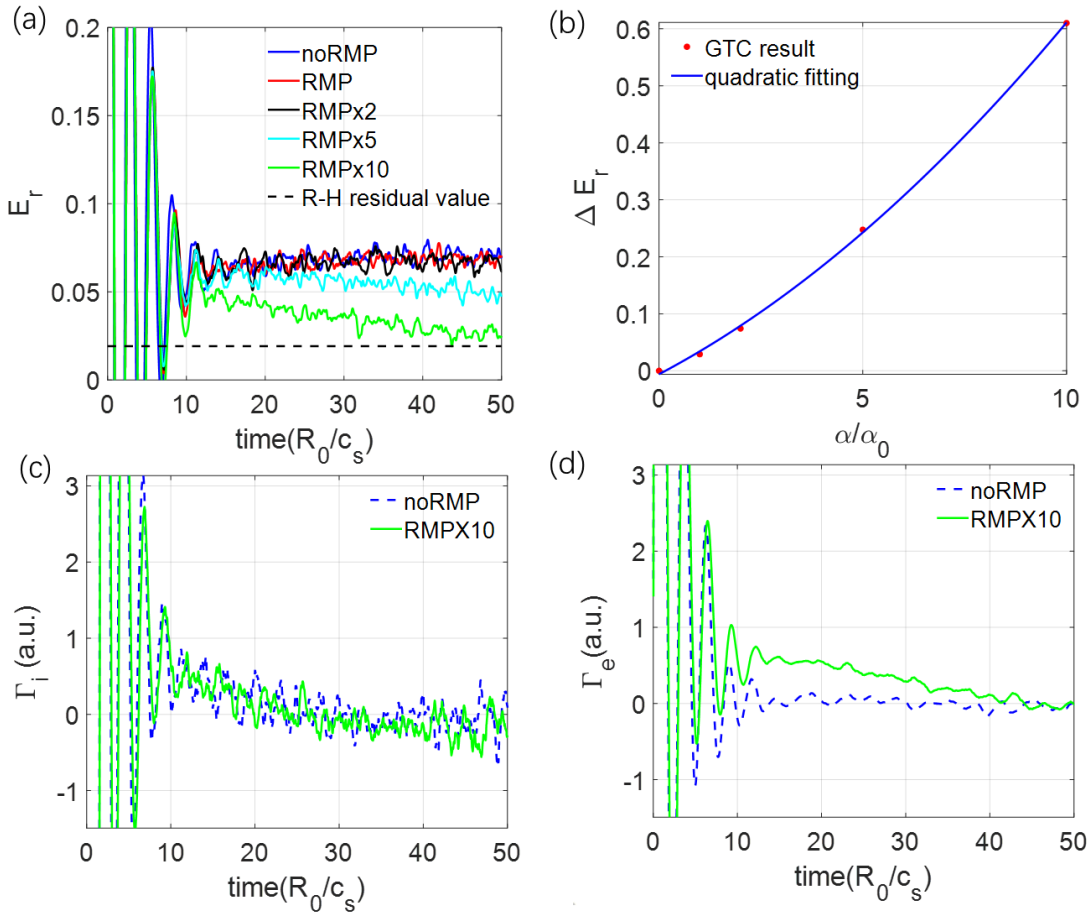

Figure 12. *In simulations using VMEC equilibrium with closed flux surfaces, time evolution of radial electric field E_r of zonal flow with kinetic electrons with various RMP amplitudes (panel a), (b) relation between change of residual flow ΔE_r at $t = 50\, R_0/c_s$ and RMP amplitude α, radial particle flux (arbitrary unit) of ion Γ_i (panel c) and electron Γ_e (panel d) during zonal flow damping process without RMP (dashed lines) and with RMP×10 (solid lines). E_r is normalized with initial value, ΔE_r is normalized with residual flow without RMP, and particle flux is normalized with value of Γ_e at $t = 10\, R_0/c_s$ in simulation with RMP×10.*

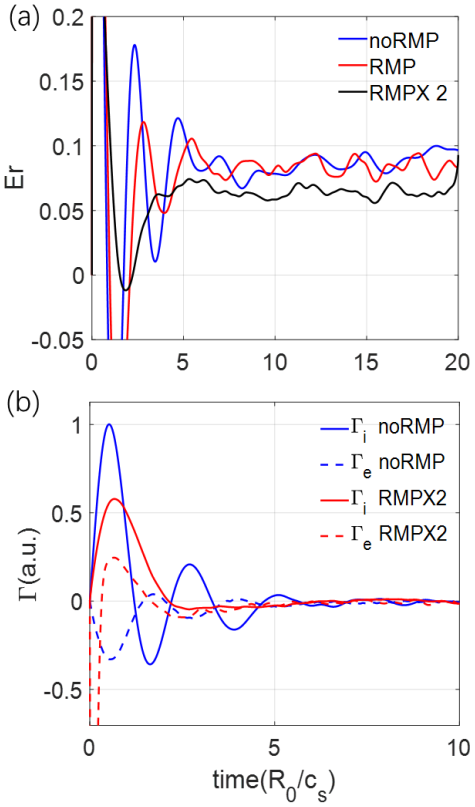

Figure 13. *Time evolution of radial electric field E_r of zonal flows (panel a), ion and electron radial particle fluxes (panel b), with various RMP amplitudes in simulations using M3D-C1 equilibrium including magnetic islands. E_r is normalized with initial value, particle fluxes are normalized with maximal value of ion particle flux Γ_i in simulation without RMP.*

II. Publications and Invited Talks

A. Publications since 2020

1. *Global gyrokinetic simulation of neoclassical ambipolar electric field and its effects on microturbulence in W7-X stellarator*, J. Y. Fu, J. H. Nicolau, P. F. Liu, X. S. Wei, Y. Xiao, and Z. Lin, *Phys. Plasmas* **28**, 062309 (2021).
2. *Effects of resonant magnetic perturbations on radial electric fields in DIII-D tokamak*, Jingyuan FU, Pengfei LIU, Xishuo WEI, Zhihong LIN, Nathaniel Mandrachia FERRAR, and Raffi NAZIKIAN, *Plasma Sci. Technol*. **23**, 105104 (2021).
3. *Global gyrokinetic simulation with kinetic electron for collisionless damping of zonal flow in stellarator*, Javier H. Nicolau, Gyungjin Choi, Jingyuan Fu, Pengfei Liu, Xishuo Wei, and Zhihong Lin, *Nuclear Fusion* **61**, 126041 (2021).
4. *Global gyrokinetic simulations of electrostatic microturbulent transport using kinetic electrons in LHD stellarator*, Tajinder Singh, Javier H Nicolau, Zhihong Lin, Sarveshwar Sharma, Abhijit Sen, Animesh Kuley, *Nuclear Fusion* **62**, 126006 (2022).

B. Invited presentations at professional conferences since 2020

2021 -- 10th US-PRC Magnetic Fusion Collaboration Workshop (online);
-- Transport Task Force Workshop (online) (plenary talks by Pengfei Liu and Javier Nicolau);
-- International Tokamak Physics Activities (ITPA) (online);
-- 47th EPS Conference on Plasma Physics (online);
-- Platform for Advanced Scientific Computing (PASC21) Conference (online).

2022 -- US-Japan JIFT Exascale Computing Workshop (online);
-- 48th EPS Conference on Plasma Physics (online, invited talk by Guillaume Brochard);
-- Technology of Fusion Energy (TOFE2022), Anaheim, CA;
-- 27th International Tokamak Physics Activities (ITPA) (online);
-- Festival de Théorie 2022, Aix-en-Provence, France;
-- 33rd IUPAP Conference on Computational Physics (online);
-- H-Mode Workshop (HMWS22) (online).